

Phaseless auxiliary-field quantum Monte Carlo method with spin-orbit coupling

Zheng Liu^{1,2}, Shiwei Zhang³, and Fengjie Ma^{1,2*}

¹*The Center for Advanced Quantum Studies and School of Physics and Astronomy,
Beijing Normal University, Beijing 100875, China*

²*Key Laboratory of Multiscale Spin Physics (Ministry of Education),
Beijing Normal University, Beijing 100875, China and*

³*Center for Computational Quantum Physics, Flatiron Institute, New York, NY 10010, USA*

(Dated: February 13, 2026)

Spin-orbit coupling (SOC) is incorporated into the phaseless plane-wave-based auxiliary-field quantum Monte Carlo (pw-AFQMC) method. This integration is implemented using optimized multiple-projector norm-conserving pseudopotentials, which are derived from the fully-relativistic (FR) atomic all-electron Dirac-like equation. The inclusion of SOC enables accurate phaseless pw-AFQMC calculations that capture both electronic correlation and SOC effects concurrently, greatly improving the method's applicability for studying systems containing heavy atoms. We discuss the form of FR pseudopotentials and detail the corresponding formulations of phaseless pw-AFQMC with a two-component Hamiltonian in the spinor basis. The accuracy of our approach is demonstrated by computing the dissociation energy of molecule I_2 and the cohesive energy of bulk Pb, highlighting the large influence of SOC in both. Subsequently, we determine the transition pressure of the III-V compound InP from its zinc-blende to rock-salt phase by constructing and analyzing their respective equations of state.

I. INTRODUCTION

Spin-orbit coupling (SOC), the relativistic interaction between an electron's spin angular momentum and its orbital motion in the nuclear electric field, is a fundamental quantum mechanical effect contributing to the electronic, magnetic, and topological properties of condensed matter systems [1–12]. Its significance is particularly prominent in compounds containing transition-metal ($3d$, $4d$, or $5d$) and rare-earth ($4f$ or $5f$) elements, where the large atomic number (Z) of constituent elements amplifies relativistic effects (scaling with Z^4) rendering SOC non-negligible for both fundamental quantum physics research and the development of emerging quantum devices [7–13]. In such systems, SOC modulates magnetic exchange interactions, spin reorientation transitions, and magnetocrystalline anisotropy—key determinants of performance in permanent magnets and spintronic devices [7–9, 14]. Stronger SOC further gives rise to exotic quantum phenomena including topological insulators, Weyl semimetals, and spin-orbit Mott insulators, where the intricate interplay of SOC, electron correlation, and band topology yields unique electronic states [3–6, 13, 15]. SOC additionally induces crystal field splitting and spin-lattice coupling, thereby enabling transformative applications in quantum sensors and optical quantum technologies [16–18]. In all these cases, SOC is not a secondary perturbation but a core driver of material functionality; its omission or insufficient theoretical treatment invariably leads to erroneous predictions of a material's structural, electronic, and magnetic properties. As demand surges for high-performance spintronic devices, topological quantum computing compo-

nents, and next-generation magnetic storage materials, a precise physical understanding and accurate theoretical description of SOC in these complex systems have become indispensable prerequisites for advancing scientific frontiers and driving technological innovation.

To date, theoretical calculations for solid-state materials are predominantly based on the traditional density functional theory (DFT) [19, 20]. Such evaluations, which rely on various mean-field approximations, often break down for systems with strong electronic correlations, however. Many-body methods that rigorously account for electronic correlations are therefore highly desired [21–24]. While the explicit incorporation of SOC into standard DFT has been very mature and the associated calculations are widely adopted [25–28], evaluations with SOC based on many-body approaches pose formidable challenges. A primary bottleneck is the prohibitive computational cost: fully-relativistic (FR) calculations that include SOC drastically expand the effective Hilbert space of the system, amplifying the inherent computational expense of many-body methods. Scalar-relativistic (SR) [29] calculations are commonly employed, as they incur nearly identical computational costs to non-relativistic (NR) calculations yet provide more accurate descriptions of heavy atoms by incorporating relativistic kinematic effects (the mass-velocity and Darwin terms) while excluding the SOC interaction. However, an ever-growing body of research has uncovered a wealth of novel quantum phenomena that emerge from the increasingly strong SOC interactions in the strongly correlated materials. As a result, SR-level calculations are no longer sufficient, and the explicit inclusion of SOC, beyond mean-field approximations has become essential. This underscores the critical need for many-body methods that rigorously and accurately treat both effects in a high-precision manner.

* fengjie.ma@bnu.edu.cn

The phaseless auxiliary-field quantum Monte Carlo (AFQMC) method [24, 30] is a powerful *ab initio* many-body electronic structure approach with a suite of advantageous features. It mitigates the fermionic sign problem (or phase instability) via the phaseless approximation based on the trial wave functions, restores low-power (typically to the third power of system size) computational scaling, and supports the use of flexible one-particle basis sets. For the description of realistic systems, the phaseless AFQMC can be formulated within two canonical one-particle basis sets: the plane-wave basis set that is ubiquitous for extended condensed matter systems [30–32], and the localized Gaussian-type basis set which is standard for atomic and molecular systems in quantum chemistry [33, 34]. One very important advantage of the plane-wave implementation with pseudopotentials is that its convergence to the basis-set limit depends uniquely and directly on the kinetic energy cutoff, enabling an unbiased representation of the wave function. The success of AFQMC method in the study of interacting many-fermion lattice models, e.g., the Hubbard model [35], highlights its capabilities for treating strong correlation. While the treatment of SOC in AFQMC has been explored for Gaussian-type orbitals [36] and model Hamiltonians [37], its integration into plane-wave-based AFQMC (pw-AFQMC) remains underdeveloped.

This work focuses on the incorporation of SOC into phaseless pw-AFQMC using optimized norm-conserving Vanderbilt (ONCV) [38] FR pseudopotentials, replacing l -dependent with j -dependent pseudopotentials for consistency with DFT procedures. The introduction of SOC requires the spins to explicitly enter the plane-wave basis which doubles the basis size, expanding the Hamiltonian into a 2×2 block matrix that mixes spins and applies to two-component spinor many-body wave functions. Related modifications for both the wave function propagation in the space of Slater determinants and the observable measurement with spinor plane-wave basis are discussed. This framework advances the many-body electronic structure method, enabling accurate treatment of both electron correlations and SOC, and extends its applicability to heavy-element-containing materials and bridges fundamental quantum physics and realistic material design.

The remainder of this paper is organized as follows. In Sec. II, we review the Hamiltonian by elaborating on each term and discuss the non-local component of pseudopotentials employed to incorporate SOC. Then we outline the theoretical framework and detailed implementations in phaseless pw-AFQMC. Section III presents the applications of the developed SOC-included phaseless pw-AFQMC approach to validate the formalism and highlight the effects of SOC. We carry out calculations for the dissociation energy of simple molecule I_2 and the cohesive energy of solid Pb, by using SR and FR pseudopotentials, respectively. The results are also compared with both DFT calculations and the experiments. We then further investigate the zinc-blende to rock-salt structural tran-

sition of a III-V compound InP. Finally, we summarize and conclude our work in Sec. IV.

II. METHODOLOGY

In this section, we begin by defining each term of the NR Hamiltonian in a plane-wave basis to establish the framework for subsequent discussions. We then elaborate on the forms of non-local pseudopotentials to incorporate SOC. Detailed implementations of phaseless pw-AFQMC, including propagation and measurement with SOC, are discussed following these.

A. Hamiltonian

The electronic Hamiltonian, separated from that of ions under the Born-Oppenheimer approximation [39], can be expressed as

$$H = K + V_{\text{e-i}} + V_{\text{e-e}} + V_{\text{II}}, \quad (1)$$

where K , $V_{\text{e-i}}$, $V_{\text{e-e}}$, and V_{II} are, respectively, the kinetic energy and electron-ion, electron-electron, and classical Coulomb ion-ion interactions [40]. The plane-wave basis (in real space representation),

$$\langle \mathbf{r} | \mathbf{k} + \mathbf{G} \rangle = \langle \mathbf{r} | c_{\mathbf{k}+\mathbf{G}}^\dagger | 0 \rangle = \frac{1}{\sqrt{\Omega}} e^{i(\mathbf{k}+\mathbf{G}) \cdot \mathbf{r}}, \quad (2)$$

is usually adopted for extended systems with periodic boundary conditions. Here, Ω denotes the volume of the simulation cell, \mathbf{G} is the reciprocal lattice vector, the vector \mathbf{k} specifies a particular choice of periodic boundary condition for the system, and $c_{\mathbf{k}+\mathbf{G}}^\dagger$ is the corresponding creation operator. We define M as the number of plane-waves within the kinetic energy cutoff and N as the number of electrons in the system.

Concretely, each term of the Hamiltonian can be further expressed in second quantization as follows. The kinetic energy, expressed as

$$K = \frac{1}{2} \sum_{\mathbf{G}, \lambda} \mathbf{G}^2 c_{\mathbf{G}, \lambda}^\dagger c_{\mathbf{G}, \lambda}, \quad (3)$$

and the pseudopotential that models the electron-ion interaction, given by

$$V_{\text{e-i}} = V^{\text{loc}} + V^{\text{nl}}, \quad (4)$$

where its local and non-local components take the forms

$$V^{\text{loc}} = \sum_{\lambda, \mathbf{G}, \mathbf{G}'} V^{\text{loc}}(\mathbf{G} - \mathbf{G}') c_{\mathbf{G}, \lambda}^\dagger c_{\mathbf{G}', \lambda}, \quad (5a)$$

$$V^{\text{nl}} = \sum_{\lambda, \mathbf{G}, \mathbf{G}'} V^{\text{nl}}(\mathbf{G}, \mathbf{G}') c_{\mathbf{G}, \lambda}^\dagger c_{\mathbf{G}', \lambda}, \quad (5b)$$

collectively form the one-body part of the Hamiltonian. We discuss details of $V^{\text{loc}}(\mathbf{G} - \mathbf{G}')$ and $V^{\text{nl}}(\mathbf{G}, \mathbf{G}')$, which represent the matrix elements corresponding to the local and non-local components of the pseudopotential, respectively, in the subsequent subsection. Both reciprocal lattice vectors \mathbf{G} and \mathbf{G}' are restricted to the basis set $\{\mathbf{G}\}$ whose size is controlled by the kinetic energy cutoff E_{cut} . Additionally, the summation over the spin index λ is written explicitly here. For brevity, any shift of the vector \mathbf{k} is omitted, as all calculations are performed at a single fixed \mathbf{k} point.

The electron-electron interaction term is

$$V_{\text{e-e}} = \frac{1}{2}N\xi + \frac{1}{2}\frac{4\pi}{\Omega} \sum_{\mathbf{Q} \neq 0} \frac{1}{Q^2} \rho^\dagger(\mathbf{Q})\rho(\mathbf{Q}) - \frac{1}{2}\frac{4\pi}{\Omega} \sum_{\lambda} \sum_{\mathbf{G} \neq \mathbf{G}'} \frac{1}{|\mathbf{G} - \mathbf{G}'|^2} c_{\mathbf{G},\lambda}^\dagger c_{\mathbf{G},\lambda}, \quad (6)$$

where the constant ξ stands for the self-interaction of an electron with its own periodic images evaluated via the standard Ewald summation method [41–43]. The third term, analogous to the kinetic energy term, corresponds to a sum of diagonal one-body operators arising from the anti-commutation of the fermion creation and annihilation operators. Here, we further introduce an important quantity, the one-body density operator

$$\rho(\mathbf{Q}) = \sum_{\lambda, \mathbf{G}} c_{\mathbf{G}-\mathbf{Q},\lambda}^\dagger c_{\mathbf{G},\lambda} \theta(E_{\text{cut}} - \frac{1}{2}|\mathbf{G} - \mathbf{Q}|^2), \quad (7)$$

where $\mathbf{Q} = \mathbf{G} - \mathbf{G}'$, and the step function θ enforces that all $(\mathbf{G} - \mathbf{Q})$'s fall within the plane-wave basis set. Correspondingly, the local potential can also be recast in terms of the one-body density operator.

It is worth emphasizing that all the aforementioned expressions are derived within the framework of a spin-unentangled Hamiltonian. In practical calculations, this allows us to work directly with the spatial plane-wave basis for each spin channel, thereby obviating the need for a rigorous spin-related expansion of the basis set.

B. Pseudopotentials

The adoption of pseudopotentials effectively eliminates core electronic states—those tightly bound to atomic nuclei, non-participating in chemical bond formation, and approximately invariant across atomic, molecular, and solid-state environments. This approximation simplifies the quantum mechanical problem to the exclusive treatment of valence electrons subject to an effective potential. Relativistic effects can be naturally incorporated into pseudopotentials, as their contribution to valence electrons arises predominantly in the nuclear-proximal interior of the atom. Widely used SR pseudopotentials are thus generated to include kinematic relativistic effects and effectively account for SOC by the construction of j -averaged pseudopotentials for each angular momentum l .

While such an approximation yields band structures with no spin-orbit splitting and is broadly acceptable for many material electronic structure calculations, it becomes inadequate in cases where observable quantities—such as hole effective masses and spin relaxation times—stem directly from spin-orbit splitting. Kleinman has shown that for valence electron wave functions outside the core region, all relativistic effects up to second order of the fine-structure constant can be captured by solving a Pauli-like Schrödinger equation with pseudopotentials derived from FR radial all-electron atomic equations [25, 44]. We henceforth refer to them as FR pseudopotentials, in analogy to the NR and SR counterparts. We initiate our discussion by outlining the formalisms of NR and SR pseudopotentials.

The plane-wave-based matrix elements corresponding to the local potential component take the form

$$V^{\text{loc}}(\mathbf{Q}) = \frac{1}{\Omega} \sum_{\gamma, \alpha} e^{-i\mathbf{Q} \cdot \mathbf{u}_{\gamma, \alpha}} V_{\alpha}^{\text{loc}}(\mathbf{Q}), \quad (8)$$

where $\mathbf{u}_{\gamma, \alpha}$ is the position vector of the γ -th atom of species α within the simulation cell, measured relative to the cell's origin. The quantity $V_{\alpha}^{\text{loc}}(\mathbf{Q})$ represents the (unnormalized) Fourier transform of the atomic local potential.

The non-local component of the pseudopotential for a given atomic species can be expressed in the separable Kleinman-Bylander form [45] (non-local in both angular and radial variables) as

$$V_{\alpha}^{\text{nl}} = \sum_{l, m} \frac{|V_{\alpha l} \varphi_{\alpha l}^{\text{ps}} Y_{lm}\rangle \langle Y_{lm} \varphi_{\alpha l}^{\text{ps}} V_{\alpha l}|}{\eta_{\alpha l}}, \quad (9)$$

where the pseudopotential $V_{\alpha l}$ and pseudo-orbital $\varphi_{\alpha l}$ rely only on the radial distance r when represented in real space, and Y_{lm} denotes the standard spherical harmonic function. The normalization factor, $\eta_{\alpha l} = \langle Y_{lm} \varphi_{\alpha l}^{\text{ps}} | V_{\alpha l} | \varphi_{\alpha l}^{\text{ps}} Y_{lm} \rangle$, is the overlap between pseudo-wavefunction and its corresponding projector $V_{\alpha l} | \varphi_{\alpha l}^{\text{ps}} Y_{lm} \rangle$. The overall matrix elements of the non-local pseudopotential take a fully separable form:

$$V^{\text{nl}}(\mathbf{G}, \mathbf{G}') = \sum_{j \in \{\gamma, \alpha, l, m\}} \frac{1}{\eta_j} F_j^*(\mathbf{G}) F_j(\mathbf{G}'), \quad (10)$$

where we introduce

$$F_j(\mathbf{G}) = \frac{4\pi}{\sqrt{\Omega}} e^{i\mathbf{G} \cdot \mathbf{u}_{\gamma, \alpha}} f_{\alpha l}(G) Y_{lm}^*(\mathbf{G}). \quad (11)$$

Here, $f_{\alpha l}(G)$ is the (radial component) Fourier transform of the projector, which can be read directly into our phaseless pw-AFQMC code.

Hamann generalized Eq. (9) to the case of multiple projectors [38] based on the framework of Vanderbilt's ultrasoft pseudopotentials (USPPs) [46]. We accordingly rewrite the non-local pseudopotential component within

the multi-projector formalism as

$$V^{\text{nl}} = \sum_{\tau, l, m} B_{l, m}^{\tau} |\chi_{\tau, l} Y_{l, m}\rangle \langle Y_{l, m} \chi_{\tau, l}|, \quad (12)$$

where $|\chi_{\tau, l}\rangle$ refers to the normalized form of the τ -th projector function $V_{\tau, \alpha l} |\varphi_{\tau, \alpha l}^{\text{ps}}\rangle$ (with only radial part). The coefficients $B_{l, m}^{\tau}$ correspond to diagonal elements of N_c -dimensional (inverse) overlap matrix $B_{i, j}$, which is constructed from projector-pseudo-wavefunction inner products and subsequently diagonalized; here, the composite indices are defined as $i = \{\tau, l\}$ and $j = \{\tau', l'\}$, and N_c is the number of total projectors, e.g., $N_c = 8$ when $l_{\text{max}} = 3$ and two projectors are assigned per l during the pseudopotential generation. Note that these coefficients typically take the form of the inverse of $1/b_i$ (following the notation in Ref. [38]) and differ from the matrix $D_{i, j}$ introduced in Refs. [28, 46], which is associated with the β functions. We retain the magnetic quantum number m in the subscript, albeit the coefficients are in fact independent of m : for a fixed l , all values of m ($-l \leq m \leq l$) share an identical $B_{l, m}^{\tau}$ for a given projector. Henceforth, we restrict our discussion to a single atom of a specified species; this simplification is justified by the fact that pseudopotential files directly provide these data (excluding the spherical harmonic component). The total non-local potential for the full system is then constructed as a simple sum of all atomic contributions, optionally weighted by the relevant atomic structure factors, as outlined in the preceding formalism.

An NR or SR pseudopotential constructed from the radial components of solutions to the corresponding-level equations depends exclusively on the orbital angular momentum l , as discussed above. The SOC effects omitted in the SR formalism can be incorporated by reformulating the pseudopotentials, with all other physical quantities remaining formally unchanged in expressions. In contrast, an FR pseudopotential depends on both the total angular momentum j and the orbital angular momentum l . Specifically, upon coupling the orbital angular momentum to a spin angular momentum of $s = 1/2$, distinct solutions arise for $j = l \pm 1/2$ when $l > 0$, whereas only $j = l + 1/2$ exists for $l = 0$. Analogous to Eq. (12), the non-local operator (for each component) now takes the form of a “ 2×2 ” matrix, given by

$$V^{\text{nl}, \lambda, \lambda'} = \sum_{\tau, l, j, m_j} B_{l, j, m_j}^{\tau} |\chi_{\tau, l, j} \tilde{Y}_{l, j, m_j}^{\lambda}\rangle \langle \tilde{Y}_{l, j, m_j}^{\lambda'} \chi_{\tau, l, j}|, \quad (13)$$

where \tilde{Y}_{l, j, m_j} are the eigenfunctions of the operator set $\{L^2, S^2, J^2, J_z\}$ (compared to $Y_{l, m}$ in $\{L^2, L_z\}$) and are commonly referred to as spin-angle functions. \tilde{Y}_{l, j, m_j} are spinor-valued, for instance, $j = l + 1/2$ adopt the form

$$\tilde{Y}_{l, j, m_j} = \begin{pmatrix} \left(\frac{l+m+1}{2l+1}\right)^{\frac{1}{2}} Y_{l, m} \\ \left(\frac{l-m}{2l+1}\right)^{\frac{1}{2}} Y_{l, m+1} \end{pmatrix}, \quad (14)$$

wherein $m = m_j - 1/2$. It is the conventional expansion with respect to the spherical harmonics and spin wave function, and the pre-factors are so-called Clebsch-Gordan coefficients. The local potential remains the j -averaged form, such that the non-local operator defined in Eq. (13) represents the sole component of the Hamiltonian responsible for spin mixing.

To incorporate SOC, we modify the pseudopotentials-reading module in our code to accommodate split j -dependent projectors and directly substitute spherical harmonics with spin-angle function to construct the non-local operator. The manner above, with a single projector, is basically equivalent to the formalism presented in Ref. [27]. We note that alternative methodologies exist for treating the non-local operator in the presence of SOC. Our discussion of FR pseudopotentials above partially follows the organizational structure of Ref. [28], wherein the coefficients of the non-local operator are first expressed in the general form ($D_{\tau, l, j, m_j; \tau', l', j', m_{j'}} = D_{\tau, \tau'}^{l, j} \delta_{l, l'} \delta_{j, j'} \delta_{m_j, m_{j'}}$). Subsequently, a unitary rotation is performed on the spherical harmonics to recast Eq. (13) into the form of Eq. (12), at the expense of breaking the diagonality. Notably, this cost does not introduce any difficulty in the implementation of USPPs. This approach to handling FR pseudopotentials of various types is implemented in the *Quantum ESPRESSO* code [47, 48]. By contrast, our implementation leverages the full diagonalities (including that between projectors) with only moderate modifications for existing multi-projector ONCV pseudopotentials in our phaseless pw-AFQMC framework [49]. One can also naturally decompose the full non-local potential into j -averaged SR and spin-orbit projectors while substituting spin-angle functions in terms of spherical harmonics [25, 26, 44], based on the relation $\mathbf{L} \cdot \mathbf{S} = l/2, -(l+1)/2$ for $j = l+1/2, l-1/2$, respectively. The ONCVPSP code [50] supports the generations of both direct j -dependent projectors $|\chi_{\tau, l, j}\rangle$ as in Eq. (13) (for *Quantum ESPRESSO* as well as our phaseless pw-AFQMC) and of separate SR and spin-orbit components (for *ABINIT* code [51]).

C. AFQMC with SOC

With the Hamiltonian formally established, we now proceed to detail the implementation of incorporating SOC into phaseless pw-AFQMC. To this end, we present and contrast theoretical frameworks and corresponding expressions with and without SOC. The formalism outlined below is universally applicable to other systems (or in a different basis set) within the AFQMC framework.

The ground-state wave function $|\phi_0\rangle$ is obtained by repeatedly applying the imaginary-time projection operator [52] to an arbitrary trial wave function $|\psi_T\rangle$ that is non-orthogonal to $|\phi_0\rangle$,

$$|\phi_0\rangle = \lim_{n \rightarrow \infty} (e^{-\Delta\tau(H - E_T)})^n |\psi_T\rangle, \quad (15)$$

where E_T is an initial estimate of the ground-state energy typically derived from $|\psi_T\rangle$. A small time-step $\Delta\tau$ facilitates the separation of one-body (H_1) and two-body (H_2) Hamiltonian components via second-order Trotter-Suzuki decomposition [53, 54]:

$$e^{-\Delta\tau H} = e^{-\frac{1}{2}\Delta\tau H_1} e^{-\Delta\tau H_2} e^{-\frac{1}{2}\Delta\tau H_1} + \mathcal{O}(\Delta\tau^3), \quad (16)$$

wherein constant Hamiltonian terms have been omitted and excluded throughout the projection process. The error introduced by a finite $\Delta\tau$ can be systematically removed by extrapolation to the limit $\Delta\tau = 0$. This decomposition scheme permits the independent treatment of each Hamiltonian component, streamlining both propagation and measurement, as well as the seamless incorporation of SOC.

1. Propagation

The propagation, namely the action of the one-body exponential propagator $B = e^{-\Delta\tau H_1}$ on a Slater determinant $|\phi\rangle$ (referred to as a walker), is operated via the multiplication of matrices $\Phi' = B\Phi$. Note that the upright, uppercase symbols B and Φ denote the corresponding matrix representations of the propagator and walker, respectively. The resulting product matrix Φ' simply leads to another Slater determinant $|\phi'\rangle$, according to Thouless theorem [55–57].

In the absence of SOC, the complete basis set can be expressible in terms of plane-waves with no spin dependence. The propagator matrix B is consequently in a dimension of $M \times M$. A random walker can be further factorized into two independent spin components, given by

$$|\phi\rangle = |\phi^\uparrow\rangle \otimes |\phi^\downarrow\rangle, \quad (17)$$

where Φ^λ , the matrix form of $|\phi^\lambda\rangle$, is of size $M \times N_\lambda$:

$$\begin{pmatrix} \varphi_{1,1}^\lambda & \varphi_{1,2}^\lambda & \cdots & \varphi_{1,N_\lambda}^\lambda \\ \varphi_{2,1}^\lambda & \varphi_{2,2}^\lambda & \cdots & \varphi_{2,N_\lambda}^\lambda \\ \vdots & \vdots & \ddots & \vdots \\ \varphi_{M,1}^\lambda & \varphi_{M,2}^\lambda & \cdots & \varphi_{M,N_\lambda}^\lambda \end{pmatrix}, \quad (18)$$

with each column vector representing a single-particle orbital $|\varphi\rangle$. Here φ_i are the coefficients in the expansion $|\varphi\rangle = \sum_i^M \varphi_i |\varepsilon_i\rangle$ in terms of basis $|\varepsilon_i\rangle$, which is the plane-wave $|\mathbf{k} + \mathbf{G}\rangle$ here. We impose that the number of electrons for each spin component is N_λ ($N_\uparrow + N_\downarrow = N$), since $S_z = N_\uparrow - N_\downarrow$ constitutes a good quantum number and can be fixed throughout the calculation.

A direct application of the two-body propagator is computationally infeasible. The Hubbard-Stratonovich (HS) transformation [58, 59] can therefore be employed to decompose the two-body propagator into a high-dimensional integral of one-body propagators over auxiliary fields

$$e^{-\Delta\tau H_2} = \left(\frac{1}{\sqrt{2\pi}}\right)^{D_\sigma} \int d\sigma e^{-\frac{1}{2}\sigma \cdot \sigma} e^{\sqrt{\Delta\tau}\sigma \cdot \mathbf{v}}, \quad (19)$$

where the vector $\sigma \equiv \{\sigma_i\}$ assembles all fields with the dimension D_σ given by the number of \mathbf{Q} vectors allowable within the basis set. The one-body operator \mathbf{v} is in linear combinations of the one-body density operator and its Hermite conjugate [30, 31].

Upon the incorporation of SOC, the primary modification is that the original M -dimensional plane-wave basis should be replaced by the generic basis, i.e., the two-component spinor plane-wave basis $|\mathbf{k} + \mathbf{G}\rangle |\lambda\rangle$ of dimension $2M$, in which $|\lambda\rangle$ denotes the spin eigenstate basis. A key consequence of SOC is that the spin components can no longer be decoupled, as the spin operator S_z no longer commutes with the Hamiltonian. Each walker Φ representing a Slater determinant is now encoded as a $2M \times N$ matrix

$$\begin{pmatrix} \varphi_{1,1} & \varphi_{1,2} & \cdots & \varphi_{1,N} \\ \varphi_{2,1} & \varphi_{2,2} & \cdots & \varphi_{2,N} \\ \vdots & \vdots & \ddots & \vdots \\ \varphi_{2M,1} & \varphi_{2M,2} & \cdots & \varphi_{2M,N} \end{pmatrix}. \quad (20)$$

By partitioning this matrix according to the “up” and “down” components in the spinor basis, the representation can be compactly rewritten in block form as

$$\Phi = \begin{pmatrix} \Phi^\uparrow \\ \Phi^\downarrow \end{pmatrix}. \quad (21)$$

This block structure directly corresponds to our practical implementation strategy, wherein the matrix is stored by appending an additional spin dimension to the basis indexing. It is important to note that the submatrix Φ^λ (each of size $M \times N$) now refers to only a component in the full Slater determinant. This stands in contrast to their interpretation in Eqs. (17) and (18) (in the non-SOC case), where Φ^λ represented the $M \times N_\lambda$ wave function matrix associated exclusively with spin- λ electrons.

Accordingly, each one-body propagator B (including those decompositions from the two-body Hamiltonian component) is of size $2M \times 2M$ and will be generalized as

$$B = \begin{pmatrix} B^{\uparrow\uparrow} & B^{\uparrow\downarrow} \\ B^{\downarrow\uparrow} & B^{\downarrow\downarrow} \end{pmatrix}. \quad (22)$$

For propagators that exhibit no spin-mixing in the pure plane-wave basis, their original $M \times M$ matrix representation B_M populates the diagonal blocks $B^{\uparrow\uparrow}$ and $B^{\downarrow\downarrow}$. As established earlier, the non-local component of the pseudopotential is the only Hamiltonian term that couples spins, implying that the off-diagonal blocks satisfy $B^{\uparrow\downarrow} = B^{\downarrow\uparrow} = 0$ for all other one-body terms. Given that each Hamiltonian component is treated independently during the propagation and measurement, terms lacking spin-mixing can retain their original non-relativistic forms without modifications. For instance, a single propagation step for these spin-diagonal terms can be realized by

$$\Phi'^\lambda = B_M \Phi^\lambda, \quad (23)$$

thereby circumventing the need to construct and manipulate a full $2M \times 2M$ matrix.

In practice, we do not even store full $M \times M$ matrices but instead exploit more efficient schemes, as direct matrix storage and multiplication incur prohibitive costs, particularly for the large basis set size of plane-waves. The kinetic energy in Eq. (3) and the exchange term in Eq. (6) are both diagonal, such that their application to the wave function reduces to simple one-dimensional array multiplications executed within a particle loop. Furthermore, fast Fourier transform (FFT) is regularly invoked for both evaluation of matrix elements and matrix multiplication, thanks to the nature of plane-waves. For example, residual one-body operators arising from the HS transformation of two-body interactions, as well as the local pseudopotential operator, can be expressed in terms of the one-body density matrix $\rho(\mathbf{Q})$ and propagated based on

$$\begin{aligned} & \exp \left[\sum_{\mathbf{Q}} \sqrt{\frac{\Delta\tau}{Q^2}} f(\mathbf{Q}) \rho(\mathbf{Q}) \right] |\phi\rangle \\ & \simeq \sum_{n=0}^{n_{\max}} \frac{1}{n!} \left[\sum_{\mathbf{Q}} \sqrt{\frac{\Delta\tau}{Q^2}} f(\mathbf{Q}) \rho(\mathbf{Q}) \right]^n |\phi\rangle, \end{aligned} \quad (24)$$

where each term in the series can be computed via iterative FFT operations, resulting in accelerated propagations. A truncation threshold of $n_{\max} \simeq 4$ is sufficient to reproduce the propagator with high fidelity for typical values of $\Delta\tau$ [31].

The non-local operator, however, presents greater challenges due to its intrinsic non-locality. We begin by taking the original j -averaged non-local operator as an illustration. As specified in Eq. (10), its matrix elements are obtained from products of $F_j(\mathbf{G})$, whose dimension is $N_j \times M$. Here, size N_j is determined by the composite index $\{\gamma, \alpha, l, m\}$. The $M \times M$ non-local potential matrix can thus be expressed as $\mathbf{V}_{\text{nl}} = \mathbf{EF}$, where the matrix elements of \mathbf{E} and \mathbf{F} correspond to $F_j^*(\mathbf{G})/\eta_j$ and $F_j(\mathbf{G})$, respectively. Its propagator is expanded as

$$\begin{aligned} \exp \left(-\frac{\Delta\tau}{2} \mathbf{V}_{\text{nl}} \right) &= \sum_{n=0} \frac{1}{n!} \left(-\frac{\Delta\tau}{2} \mathbf{V}_{\text{nl}} \right)^n \\ &= \mathbf{I} + \mathbf{E} \left[\sum_{n=1} \frac{1}{n!} \left(-\frac{\Delta\tau}{2} \right)^n \mathbf{A}^{n-1} \right] \mathbf{F}, \end{aligned} \quad (25)$$

where \mathbf{I} is the identity matrix and $\mathbf{A} = \mathbf{FE}$ is a compact matrix of size $N_j \times N_j$. (Usually we sum up to $n = 20$.) This replacement from \mathbf{EF} ($M \times M$) to \mathbf{FE} ($N_j \times N_j$) yields substantial savings in both storage and computational cost, as it obviates the need to directly exponentiate the large $M \times M$ matrix or apply it to the walker. In the propagation step, we compute the product $\mathbf{F}\mathbf{F}$ first to leverage this dimensional reduction.

Following the incorporation of SOC into the non-local operator (cf. Eq. (13)), its matrix elements take a form

analogous to Eq. (10) but now carry an explicit spin dependence. This spin dependence is encoded as

$$F_J(\mathbf{G}, \lambda) = \frac{4\pi}{\sqrt{\Omega}} e^{i\mathbf{G} \cdot \mathbf{u}_{\gamma, \alpha}} f_{\alpha, l, j}(G) \tilde{Y}_{l, j, m_j}^{\lambda*}, \quad (26)$$

where the composite index J is extended to $\{\gamma, \alpha, l, j, m_j\}$. The construction of the SOC-inclusive propagator follows the same procedure as that outlined in Eq. (25), with the key distinction that the matrix blocks (each of size $M \times M$) are populated according to four distinct spin configurations. The propagation is then executed within a spin-resolved loop.

2. Measurement

Observable measurement, performed on the converged ground-state wave function, in conjunction with the propagation, form the complete phaseless pw-AFQMC algorithm. The mixed estimator is always exploited to calculate the ground-state energy

$$E_0 = \frac{\langle \psi_T | H | \phi \rangle}{\langle \psi_T | \phi \rangle}. \quad (27)$$

Measurements are carried out via evaluating the Green's function [60]

$$G_{ji} = \frac{\langle \psi | c_i^\dagger c_j | \phi \rangle}{\langle \psi | \phi \rangle} = [\Phi(\Psi^\dagger \Phi)^{-1} \Psi^\dagger]_{ji}. \quad (28)$$

In standard implementations, the state $\langle \psi |$ is taken as the trial wave function $\langle \psi_T |$; however, it can be replaced by any arbitrary Slater determinant, such as in back-propagation schemes [60–62].

For any one-body operator, for instance the kinetic energy, its estimator can be expressed as

$$\langle K \rangle = \frac{1}{2} \sum_{\lambda} \sum_i^M \mathbf{G}_i^2 G_{ii}^{\lambda\lambda}, \quad (29)$$

where in general $G_{ji}^{\lambda\lambda'} = \langle \psi_T | c_{i,\lambda}^\dagger c_{j,\lambda} | \phi \rangle / \langle \psi_T | \phi \rangle$ are the elements of this $2M \times 2M$ matrix, which can be divided into four spin-resolved subblocks corresponding to all spin index combinations. For example, the upper-right (1, 2) subblock contains the matrix elements associated with $\uparrow\downarrow$ spin-flip processes.

By applying Wick's theorem [63], the two-body electron-electron energy is estimated by

$$\langle V_{\text{e-e}} \rangle = \frac{1}{2} \sum_{\lambda\lambda'} \sum_{ijkl}^M V_{\text{ee}}^{ijkl} (G_{il}^{\lambda\lambda} G_{jk}^{\lambda'\lambda'} - G_{ik}^{\lambda\lambda'} G_{jl}^{\lambda'\lambda}), \quad (30)$$

where V_{ee}^{ijkl} denotes the two-body matrix elements. The first term in parentheses corresponds to the direct (Coulomb) term, and the second to the cross (exchange) term.

In the absence of SOC, there are no spin-flip operators of the form $c_{i,\lambda'}^\dagger c_{j,\lambda}$ for $\lambda \neq \lambda'$, and Green's function $G_{ij}^{\lambda\lambda'} = 0$ for $\lambda \neq \lambda'$. In other words, the off-diagonal parts vanish rendering the matrix block-diagonal. The cross term is consequently reduced to a single spin index summation. Moreover, since the wave function is factorized into independent spin-up and spin-down components, the Green's function can be computed by $G_{ji}^\lambda = [\Phi^\lambda (\Psi^{\lambda\dagger} \Phi^\lambda)^{-1} \Psi^{\lambda\dagger}]_{ji} = G_{ji}^{\lambda\lambda}$.

It is natural to decompose the Green's function and pre-compute

$$\Theta_{jq}^\lambda = [\Phi^\lambda (\Psi^{\lambda\dagger} \Phi^\lambda)^{-1}]_{jq}, \quad (31)$$

which possesses the same dimensionality as a random walker matrix. The Green's function then takes the form

$$G_{ji}^\lambda = \sum_q^{N_\lambda} \Theta_{jq}^\lambda \Psi_{iq}^{\lambda*}, \quad (32)$$

where i and j index the basis vectors and q denotes the particle index. For subsequent calculations, we additionally define the real-space representations via (inverse) Fourier transformation: $\tilde{\Theta}_{\mathbf{r}q}^\lambda = \sum_j e^{i\mathbf{G}_j \cdot \mathbf{r}} \Theta_{jq}^\lambda$ and $\tilde{\Psi}_{\mathbf{r}q}^{\lambda*} = \sum_j e^{-i\mathbf{G}_j \cdot \mathbf{r}} \Psi_{iq}^{\lambda*}$. (A tilde is affixed to the symbols here to denote their real-space form.)

We address measurement by detailing the mixed-estimator of the cross term in this part. The matrix elements of the two-body term in the plane-wave basis are given by

$$V_{ee}^{ijkl} = \langle \mathbf{k} + \mathbf{G}_i, \mathbf{k} + \mathbf{G}_j | V_{e-e} | \mathbf{k} + \mathbf{G}_l, \mathbf{k} + \mathbf{G}_k \rangle = \frac{4\pi}{\Omega} \sum_{\mathbf{Q}} \frac{1}{Q^2} \int \frac{d\mathbf{r}}{\Omega} e^{-i(\mathbf{Q} + \mathbf{G}_l - \mathbf{G}_i) \cdot \mathbf{r}} \int \frac{d\mathbf{r}'}{\Omega} e^{i(\mathbf{Q} - \mathbf{G}_k + \mathbf{G}_j) \cdot \mathbf{r}'} \quad (33)$$

The wave vector \mathbf{k} is explicitly retained in this expression; as with the local pseudopotential matrix elements, however, it does not play a role here. The mixed estimator of the cross term is then

$$\langle V_{e-e}^{\text{ex}} \rangle = \frac{1}{2} \frac{4\pi}{\Omega} \sum_{\mathbf{Q}} \frac{1}{Q^2} \sum_{\lambda} \sum_{qq'} \int \frac{d\mathbf{r}}{\Omega} e^{-i\mathbf{Q} \cdot \mathbf{r}} \tilde{\Theta}_{\mathbf{r}q}^\lambda \tilde{\Psi}_{\mathbf{r}q'}^{\lambda*} \int \frac{d\mathbf{r}'}{\Omega} e^{i\mathbf{Q} \cdot \mathbf{r}'} \tilde{\Theta}_{\mathbf{r}'q'}^{\lambda} \tilde{\Psi}_{\mathbf{r}'q}^{\lambda*}. \quad (34)$$

By introducing $\tilde{F}_x^\lambda(\mathbf{r}, q, q') = \tilde{\Theta}_{\mathbf{r}q}^\lambda \tilde{\Psi}_{\mathbf{r}q'}^{\lambda*}$ and its Fourier transform $F_x^\lambda(\mathbf{Q}, q, q')$, we can decompose the cross term into diagonal ($q = q'$) and off-diagonal ($q \neq q'$) contributions, followed by straightforward summations over the particle and spin indices.

The direct term is more straightforward to evaluate. As its formulation involves no index exchange or entanglement in the Green's function, and the summation runs over the two spins independently, we can compute

it solely by evaluating $\tilde{F}_d(\mathbf{r}) = \sum_{\lambda,q} \tilde{\Theta}_{\mathbf{r}q}^\lambda \tilde{\Psi}_{\mathbf{r}q}^{\lambda*}$ (and its corresponding Fourier transform).

Accordingly, we can always treat spin-up and spin-down independently in both wave function propagation and observable measurement steps to perform spin-polarized or spin-unpolarized (including restricted case, i.e., orbitals with minority spin are identical to those with majority spin) calculations.

In the spinor basis, original spin-independent terms in the Hamiltonian remain block-diagonal and can be propagated separately for “up” and “down”, as prescribed by Eq. (23). The Green's function in identical form as Eq. (22), however, is always a full $2M \times 2M$ matrix due to the generic walker being represented as a $2M \times N$ matrix in the spinor basis. Our preceding implementation framework can be preserved with only minor modifications via the redefinition

$$\Theta_{jq}^\lambda = [\Phi^\lambda (\Psi^{\lambda\dagger} \Phi^\lambda)^{-1}]_{jq}, \quad (35)$$

where Φ^λ is defined as in Eq. (21). The cross term to the two-body electron-electron energy and the non-local potential with SOC included require additional reformulations, while the estimation of all other terms in the Hamiltonian follows identical procedures as before. Since the cross term now involves a double summation over spin indices, we can somewhat simplify Eq. (34) by introducing

$$\tilde{F}_x(\mathbf{r}, q, q') = \sum_{\lambda} \tilde{\Theta}_{\mathbf{r}q}^\lambda \tilde{\Psi}_{\mathbf{r}q'}^{\lambda*}, \quad (36)$$

in which the spin summation is performed internally. The non-local operators involve a double summation over spins (combined with basis sets) as well and can be estimated individually in a similar manner.

All other relevant quantities in the simulation, e.g., the propagation of the weight, force bias, and mean-field background [30, 32], can be evaluated using estimators constructed following the procedures outlined above.

III. APPLICATIONS

To elucidate the effects of SOC, a clean and instructive example is to calculate the relative binding energies of simple atomic or molecular systems, specifically for heavy p -block elements [64–66], with and without SOC included, respectively. In this section, we first apply our phaseless pw-AFQMC method to two benchmark cases: the dissociation energy of molecule I_2 and the cohesive energy of crystalline Pb. Our results are benchmarked against available experimental data and compared with corresponding DFT calculations for reference. We then employ phaseless pw-AFQMC with SOC to compute the equations of state (EOS) for the zinc-blende (ZB) and rock-salt (RS) phases of the III-V compound InP, and determine the phase transition pressure between these two phases. All DFT calculations were performed using the *Quantum ESPRESSO* package [47, 48].

A. I_2 and Pb

Halogen elements with high atomic number are well known to exhibit strong SOC effects [66], e.g., post- d elements Br and I, which have been widely studied in chemistry. We take the molecule I_2 as an illustration and calculate its dissociation energy as $D_e = 2E_{\text{atom}} - E_{\text{mol}}$, where E_{atom} and E_{mol} are the ground state energies of the isolated atom and molecule, respectively. The molecular energy of I_2 is evaluated at the experimental equilibrium bond length of 2.666 Å [67]. For all plane-wave-based calculations, we employ (SR and FR) local density approximation (LDA) pseudopotentials, generated from the atomic reference state $[\text{Pd}]5s^25p^5$ using the ONCVPSP code [50]. Both DFT and phaseless pw-AFQMC calculations for the iodine atom and I_2 molecule are performed at the single $\mathbf{k} = \Gamma$ point, within a large cubic simulation cell of size $L = 12$ Å. In phaseless pw-AFQMC calculations, the trial wave function adopts the simplest form, of the corresponding DFT-LDA ground-state wave function.

The results with and without SOC from DFT-LDA and phaseless pw-AFQMC are presented in Fig. 1, where the postprocessing finite-size correction scheme [68, 69] is applied to both atomic and molecular energies from the phaseless pw-AFQMC calculations (although these corrections nearly cancel out in the D_e). The experimental reference bar for the non-SOC case (left-hand cluster) is obtained by approximate removal of SOC effects [70] from the measured experimental dissociation energy [67], and is included here for direct comparison. Compared to this “ j -averaged” experimental value, non-SOC DFT-LDA and phaseless pw-AFQMC calculations overestimate the dissociation energy by 0.50 and 0.06(3) eV, respectively. After the inclusion of SOC, DFT-LDA overestimates the energy by 0.59 eV, while phaseless pw-AFQMC result is in excellent agreement with the experimental value within the statistical uncertainty. Our phaseless pw-AFQMC calculations of I_2 also yield results that are in accord with those reported in Ref. [36] at both relativistic levels, where the latter study was performed using a Gaussian basis set.

For atom I in a spin-polarized calculation without SOC, it has an open-shell electronic configuration $5s^25p^5$ with 4 \uparrow and 3 \downarrow electrons, implying that a degeneracy exists for the 2 \downarrow electrons in the p -orbitals. This degeneracy is treated via fractional occupations in DFT-LDA calculations, with 2/3 of a \downarrow electron assigned to each p -orbital. For phaseless pw-AFQMC calculations, in contrast, initializing from a single-determinant trial wave function—for instance, partially populating two of the three p -orbitals with the 2 \downarrow electrons—explicitly breaks the three-fold symmetry of the p -orbital manifold. Additionally, the phaseless approximation, which uses the trial wave function to guide walkers’ evolution, may compromise the numerical accuracy of the results to a certain extent. To explore this potential issue in greater depth, we constructed a more symmetric

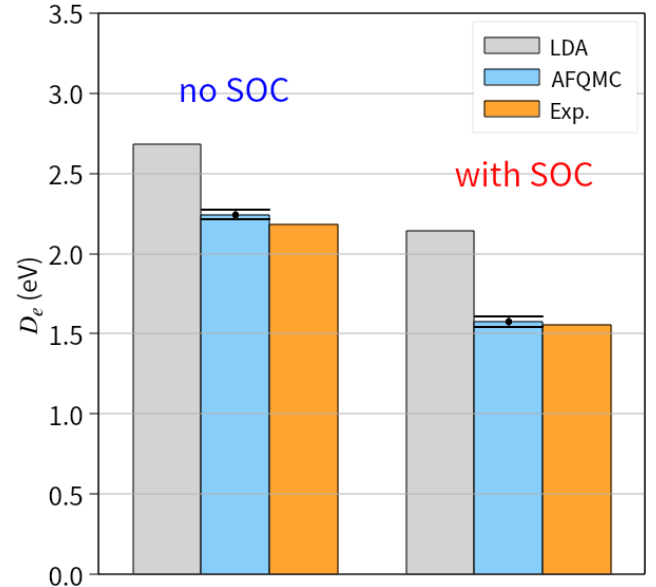


FIG. 1. Dissociation energy of molecule I_2 from SR (labeled “no SOC”) and FR (labeled “with SOC”) calculations, comparing the results from DFT-LDA (gray bins), phaseless pw-AFQMC (blue bins) and experiment (orange bins). Statistical uncertainties for the phaseless pw-AFQMC calculations are represented by black horizontal error bars.

multi-determinant trial wave function that incorporates all three p -orbitals, generated by equally weighting linear combinations of any two p -orbitals for the 2 \downarrow electrons. As discussed in Ref. [31], however, the resulting phaseless pw-AFQMC results show no appreciable deviations and agree with those from the single-determinant approach within statistical error bars. In other words, here the multi-determinant trial wave function presents results of equivalent quality to the single-determinant trial wave function.

We then turn our attention to bulk materials, of another substantially heavier element Pb with a large atomic number ($Z = 82$). Here we focus on the cohesive energy defined as $E_{\text{coh}} = E_{\text{atom}} - E_{\text{sol}}$, which is obtained by calculating the ground-state energy of an isolated Pb atom (E_{atom}) and the per-atom ground-state energy of solid Pb (E_{sol}). For both SR and FR calculations, non-local LDA-type pseudopotentials are employed, with the $5d^{10}6s^26p^2$ electrons treated as valence states [71]. The isolated Pb atom is simulated within a cubic supercell of $L = 10$ Å, while bulk face-centered cubic (fcc) Pb is modeled using the experimental lattice constant $a_0 = 4.95$ Å.

Fig. 2 presents the cohesive energy results from the DFT-LDA and phaseless pw-AFQMC calculations, with the experimentally measured value denoted in the right-hand cluster [72]. In phaseless pw-AFQMC calculations, we use the hybrid formalism [30, 32] for both the atom and bulk crystal, where a 4-atom cubic supercell is adopted for bulk Pb. A single Γ \mathbf{k} -point is used for the atom in both DFT-LDA and phaseless pw-AFQMC

calculations. For fcc bulk Pb, the DFT-LDA calculations sample the Brillouin zone using a dense $16 \times 16 \times 16$ Monkhorst-Pack \mathbf{k} grid [73] for the primitive cell, whereas phaseless pw-AFQMC calculations employ a single representative Baldereschi mean-value \mathbf{k} point [74] for cubic cell. Finite-size error corrections accounting for one-body and two-body contributions are additionally applied to the phaseless pw-AFQMC results. In the SR case without SOC, both DFT-LDA (3.82 eV) and phaseless pw-AFQMC (3.71(4) eV) overestimate the experimental cohesive energy and the corresponding results including SOC by over 1 eV, confirming the inherently strong SOC effects in Pb as anticipated. Upon the inclusion of SOC, the DFT-LDA value deviates from the experimental value by about 0.49 eV, while the phaseless pw-AFQMC calculation reduces this discrepancy to a mere 0.07(5) eV.

While the good agreement between the phaseless pw-AFQMC results and experimental measurements is encouraging, our present treatment of bulk Pb adopts several simplifications. First, a larger supercell would be necessary to minimize finite-size errors as thoroughly as possible. Second, due to the metallicity of solid Pb, the use of twist-averaged boundary conditions instead of a single Baldereschi point would be more appropriate. These two factors are expected to largely counteract one another. Additionally, the experimental lattice constant and cohesive energy values used in this work are taken from different references, which may introduce a small systematic bias as well. Importantly, none of these simplifications should affect the subsequent analysis of SOC effects presented in this study. In DFT-LDA calculations, the inclusion of SOC reduces the cohesive energy by about 1.30 eV, whereas this reduction amounts to as much as 1.61(7) eV in phaseless pw-AFQMC calculations. This disparity uncovers the intricate interplay between electronic correlation and SOC effects in Pb.

B. Transition pressure of InP

Predicting the transition pressure of materials constitutes a stringent benchmark for theoretical total-energy methods, as it requires high precision in the calculation of relative energies. For prototypical III-V compounds, the structure-property transformation (e.g. semiconductor to metal) with substantial volume collapse that accompanies pressure-induced transitions has been extensively investigated [77, 81]. Here we focus on indium phosphide (InP), a III-V compound containing heavy element In, and employ our developed phaseless pw-AFQMC with SOC method to investigate its structural phases. Solid InP serves as an ideal model system owing to its pressure-driven phase transition from the ZB to the RS phase with both structures possessing only a single structural variable parameter (the lattice constant), enabling comprehensive characterization of the transition via our phaseless pw-AFQMC calculations.

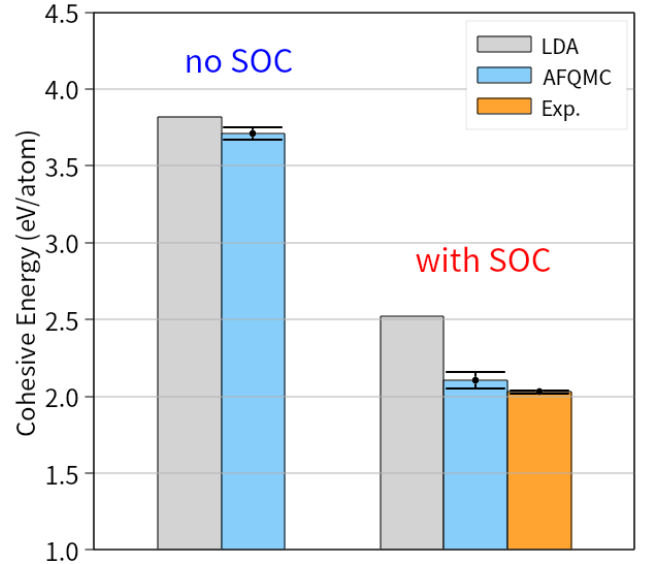


FIG. 2. Cohesive energy of bulk Pb. DFT-LDA and phaseless pw-AFQMC results are displayed as gray and blue bins, respectively. Finite-size correction has been applied to the phaseless pw-AFQMC results. The orange bin with an error bar represents the experimental value with its associated uncertainty. Black horizontal bars on blue bins represent the stochastic uncertainties of the phaseless pw-AFQMC calculations.

For both DFT and phaseless pw-AFQMC calculations, the FR pseudopotentials of In and P are generated using generalized gradient approximation (GGA) with the Perdew-Burke-Ernzerhof (PBE) [82] exchange-correlation functional. A “large-core” pseudopotential retaining the $5s^25p^1$ valence states is adopted for In, whereas P used a neon-core pseudopotential. In phaseless pw-AFQMC calculations for both structures, a four-formula cubic supercell is used with the twist boundary condition corresponding to the Baldereschi \mathbf{k} point. The fitted EOSs curves via the third-order Birch-Murnaghan equation [83] are presented in Fig. 3. The equilibrium lattice constant and the bulk modulus obtained from our phaseless pw-AFQMC and corresponding DFT calculations, alongside results from other theoretical and experimental works for comparison, are summarized in Table I. Taking the ZB phase as an illustration, it can be seen that standard GGA calculations systematically overestimate the equilibrium lattice constant, while LDA gives a slight underestimation. For the bulk modulus, the calculated value by LDA is consistent with the experiment, whereas those calculated by GGA are substantially underestimated. Notably, despite LDA’s accurate prediction of structural parameters, the phase transition pressure computed via LDA is more than 3 GPa lower than the experimental value. By contrast, the transition pressure obtained from GGA calculations is in better agreement with experimental measurements than that from LDA. Compared with these theoretical and experimen-

TABLE I. Structural properties of the ZB and RS phases of InP, along with the transition pressure P_t (GPa) between the two phases. Here, a_0 (Å) is the equilibrium lattice constant and B_0 (GPa) is the zero-pressure bulk modulus. Theoretical works with LDA and GGA exchange-correlation functionals from other references are based on all-electron calculations. Also presented for comparison are our DFT results obtained using the same pseudopotentials as those employed in phaseless pw-AFQMC (SOC-AFQMC) calculations. Fitting uncertainties for the phaseless pw-AFQMC calculations are given in parentheses.

	ZB structure		RS structure		
	a_0 (Å)	B_0 (GPa)	a_0 (Å)	B_0 (GPa)	P_t (GPa)
Experiment	5.869 ^a , 5.858 ^f	76(4) ^b , 72.0 ^f			9.8(5) ^c , 10.8 ^b
LDA	5.838 ^d	72.06 ^d	5.428 ^d	92.06 ^d	6.37 ^d
GGA	6.00 ^e	62.39 ^e	5.55 ^e	79.12 ^e	7.35 ^e , 8.90 ^d
GGA (This work)	5.948	58.0	5.538	75.2	7.60
SOC-AFQMC	5.887(1)	72.0(4)	5.488(7)	87(3)	8.85(17)

^a Reference [75].

^b Reference [76].

^c Reference [77].

^d Reference [78].

^e Reference [79].

^f Reference [80]. Zero-point effects are removed.

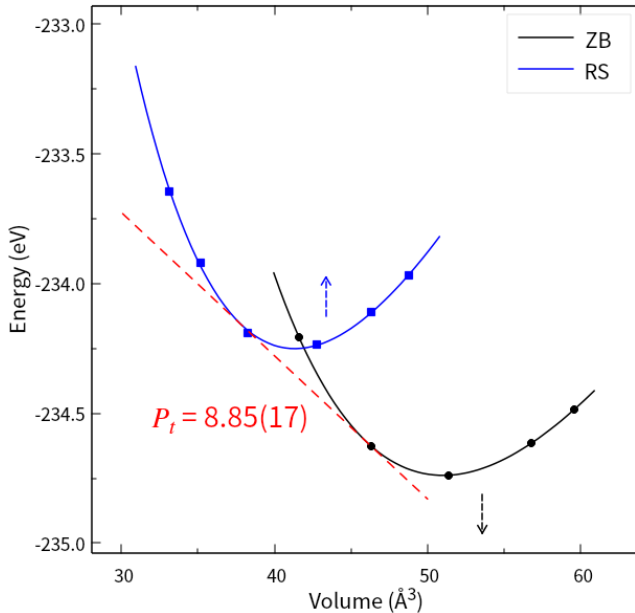


FIG. 3. Equation of state curves for ZB (black solid lines) and RS (blue solid lines) phases of InP (fitted to the third-order Birch-Murnaghan equation). Filled circles (ZB) and squares (RS) correspond to the calculated data from phaseless pw-AFQMC, with the associated stochastic errors being smaller than the marker size. All values, obtained using cubic supercell, are converted to the one-formula primitive cell for consistency in presentation. The red dashed line denotes the common tangent to the two EOS curves and its (negative) slope represents the transition pressure P_t , where the value in parentheses denotes the statistical error during fittings. Arrows indicate the direction of residual finite-size errors, as discussed in the main text.

tal results, the phaseless pw-AFQMC calculations yield high-accuracy structural properties for the (ZB) phase—in closer accord with LDA results—while delivering a far more reliable prediction of the phase transition pressure that is comparable to the GGA result. We also provide a qualitative analysis of the underlying origin for this behavior: LDA’s accurate estimation of structural parameters (assumed to hold for the RS phase as well) yet poor prediction of the transition pressure is most possibly attributed to an inherent bias in its evaluation of the relative total energy between the two phases.

The visible discrepancy between the phaseless pw-AFQMC-predicted phase transition pressure and experimental measurements can be attributed to the simplified computational treatments employed in this work. First and foremost, residual finite-size errors persist for both phases and exhibit opposing trends in their respective effects. We additionally repeated calculations using a one-formula primitive fcc cell, and the predicted structural parameters are reasonably satisfactory but with a low transition pressure of only ~ 7.2 GPa. A comparison of the EOS curves for cubic versus primitive cells across both phases reveals that the larger supercell elevates the overall EOS curve for the RS phase while lowering that of the ZB phase, as indicated by the arrows in Fig. 3, consequently increasing and improving the predicted transition pressure. Second, since InP is metallic in the RS phase, a denser sampling of random twist-angles would be required to achieve a rigorous, high-accuracy treatment of this phase. Furthermore, incorporating the semi-core 4d states into the In pseudopotential may potentially yield further improvements, as indicated by the slight discrepancy compared to those from referenced all-electron calculations (third row in Table I) in DFT level.

IV. SUMMARY

We have explicitly incorporated SOC into the many-body phaseless pw-AFQMC method, and this implementation extends the capabilities of our approach to enable more accurate descriptions of heavy-element-containing systems beyond the SR approximation. This advancement is achieved by expanding the single-particle basis in a complete set of two-component spinor plane-wave basis and employing the FR ONCV pseudopotentials that inherently account for SOC effects. We discussed the formalisms within this framework, and outlined the implementation of phaseless pw-AFQMC with and without SOC. To demonstrate the effects of SOC, we apply the phaseless pw-AFQMC method to calculate the dissociation energy of molecule I_2 and the cohesive energy of bulk Pb at both the SR and FR levels. Our calculated results are in good agreement with experimental measurements. Finally, we computed the structural proper-

ties of the III-V compound InP in its ZB and RS phase. Our predicted structural properties for the ZB phase are in excellent agreement with experimental values, while the calculated phase transition pressure between the two phases is slightly beneath the experimental result. This deviation is primarily attributed to the distinct finite-size scaling behaviors of the two structures, for which recent advances, e.g., to impose \mathbf{k} -symmetry, improve computational efficiency, and implement GPU accelerations, can be easily incorporated.

ACKNOWLEDGMENTS

This work was financially supported by the National Natural Science Foundation of China (Grants No. 12074040 and No. 11674027). F. Ma was also supported by the BNU Tang Scholar. The Flatiron Institute is a division of the Simons Foundation. Computing was carried out through the support from the Center for Advanced Quantum Studies, Beijing Normal University.

[1] J. D. Jackson, Classical electrodynamics, 3rd ed. (Wiley, Hoboken, New Jersey, 1998).

[2] E. Y. Tsymbal and I. Žutić (eds.), Spintronics handbook, 2nd ed. (CRC Press, Boca Raton, FL, 2019).

[3] F. D. M. Haldane, *Rev. Mod. Phys.* **89**, 040502 (2017).

[4] X.-L. Qi and S.-C. Zhang, *Rev. Mod. Phys.* **83**, 1057 (2011).

[5] M. Z. Hasan and C. L. Kane, *Rev. Mod. Phys.* **82**, 3045 (2010).

[6] N. P. Armitage, E. J. Mele, and A. Vishwanath, *Rev. Mod. Phys.* **90**, 015001 (2018).

[7] Y. Matsuda, T. Shibauchi, and H.-Y. Kee, *Rev. Mod. Phys.* **97**, 045003 (2025).

[8] V. Baltz, A. Manchon, M. Tsoi, T. Moriyama, T. Ono, and Y. Tserkovnyak, *Rev. Mod. Phys.* **90**, 015005 (2018).

[9] I. Žutić, J. Fabian, and S. Das Sarma, *Rev. Mod. Phys.* **76**, 323 (2004).

[10] J. S. Gardner, M. J. P. Gingras, and J. E. Greidan, *Rev. Mod. Phys.* **82**, 53 (2010).

[11] A. P. Petrović, C. Psaroudaki, P. Fischer, M. Garst, and C. Panagopoulos, *Rev. Mod. Phys.* **97**, 031001 (2025).

[12] C.-Z. Chang, C.-X. Liu, and A. H. MacDonald, *Rev. Mod. Phys.* **95**, 011002 (2023).

[13] K. W. Plumb, J. P. Clancy, L. J. Sandilands, V. V. Shankar, Y. F. Hu, K. S. Burch, H.-Y. Kee, and Y.-J. Kim, *Phys. Rev. B* **90**, 041112 (2014).

[14] X. Xu, W. Yao, D. Xiao, and T. F. Heinz, *Nature Physics* **10**, 343 (2014).

[15] N. Reyren, S. Thiel, A. D. Caviglia, L. F. Kourkoutis, G. Hammerl, C. Richter, C. W. Schneider, T. Kopp, A.-S. Rüetschi, D. Jaccard, M. Gabay, D. A. Muller, J.-M. Triscone, and J. Mannhart, *Science* **317**, 1196 (2007).

[16] J. Ye and P. Zoller, *Phys. Rev. Lett.* **132**, 190001 (2024).

[17] C. L. Degen, F. Reinhard, and P. Cappellaro, *Rev. Mod. Phys.* **89**, 035002 (2017).

[18] N. Banerjee, C. Bell, C. Ciccarelli, T. Hesjedal, F. Johnson, H. Kurebayashi, T. A. Moore, C. Moutafis, H. L. Stern, I. J. Vera-Marun, J. Wade, C. Barton, M. R. Connolly, N. J. Curson, K. Fallon, A. J. Fisher, D. A. Gangloff, W. Griggs, E. Linfield, C. H. Marrows, A. Rossi, F. Schindler, J. Smith, T. Thomson, and O. Kazakova, *Applied Physics Reviews* **12**, 041328 (2025).

[19] P. Hohenberg and W. Kohn, *Phys. Rev.* **136**, B864 (1964).

[20] W. Kohn and L. J. Sham, *Phys. Rev.* **140**, A1133 (1965).

[21] P. R. C. Kent and G. Kotliar, *Science* **361**, 348 (2018).

[22] W. M. C. Foulkes, L. Mitas, R. J. Needs, and G. Rajagopal, *Rev. Mod. Phys.* **73**, 33 (2001).

[23] A. Georges, G. Kotliar, W. Krauth, and M. J. Rozenberg, *Rev. Mod. Phys.* **68**, 13 (1996).

[24] M. Motta and S. Zhang, *WIREs Computational Molecular Science* **8**, e1364 (2018).

[25] G. B. Bachelet and M. Schlüter, *Phys. Rev. B* **25**, 2103 (1982).

[26] L. A. Hemstreet, C. Y. Fong, and J. S. Nelson, *Phys. Rev. B* **47**, 4238 (1993).

[27] G. Theurich and N. A. Hill, *Phys. Rev. B* **64**, 073106 (2001).

[28] A. D. Corso and A. M. Conte, *Phys. Rev. B* **71**, 115106 (2005).

[29] D. D. Koelling and B. N. Harmon, *Journal of Physics C: Solid State Physics* **10**, 3107 (1977).

[30] S. Zhang and H. Krakauer, *Phys. Rev. Lett.* **90**, 136401 (2003).

[31] M. Suewattana, W. Purwanto, S. Zhang, H. Krakauer, and E. J. Walter, *Phys. Rev. B* **75**, 245123 (2007).

[32] W. Purwanto, H. Krakauer, and S. Zhang, *Phys. Rev. B* **80**, 214116 (2009).

[33] W. A. Al-Saidi, S. Zhang, and H. Krakauer, *The Journal of Chemical Physics* **124**, 224101 (2006).

[34] W. Purwanto, H. Krakauer, Y. Virgus, and S. Zhang, *The Journal of Chemical Physics* **135**, 164105 (2011).

[35] S. Zhang, J. Carlson, and J. E. Gubernatis, *Phys. Rev. B* **55**, 7464 (1997).

[36] B. Eskridge, H. Krakauer, H. Shi, and S. Zhang, *The Journal of Chemical Physics* **156**, 014107 (2022).

[37] P. Rosenberg, H. Shi, and S. Zhang, *Journal of Physics and Chemistry of Solids* **128**, 161 (2019).

[38] D. R. Hamann, *Phys. Rev. B* **88**, 085117 (2013).

[39] M. Born and R. Oppenheimer, *Annalen der Physik* **389**, 457 (1927).

[40] M. T. Yin and M. L. Cohen, *Phys. Rev. B* **26**, 3259 (1982).

[41] L. M. Fraser, W. M. C. Foulkes, G. Rajagopal, R. J. Needs, S. D. Kenny, and A. J. Williamson, *Phys. Rev. B* **53**, 1814 (1996).

[42] P. P. Ewald, *Annalen der Physik* **369**, 253 (1921).

[43] R. Martin, *Electronic structure: Basic theory and practical methods* (Cambridge University Press, 2020).

[44] L. Kleinman, *Phys. Rev. B* **21**, 2630 (1980).

[45] L. Kleinman and D. M. Bylander, *Phys. Rev. Lett.* **48**, 1425 (1982).

[46] D. Vanderbilt, *Phys. Rev. B* **41**, 7892 (1990).

[47] P. Giannozzi, S. Baroni, N. Bonini, M. Calandra, R. Car, C. Cavazzoni, D. Ceresoli, G. L. Chiarotti, M. Cococcioni, I. Dabo, A. Dal Corso, S. de Gironcoli, S. Fabris, G. Fratesi, R. Gebauer, U. Gerstmann, C. Gougaussis, A. Kokalj, M. Lazzeri, L. Martin-Samos, N. Marzari, F. Mauri, R. Mazzarello, S. Paolini, A. Pasquarello, L. Paulatto, C. Sbraccia, S. Scandolo, G. Sclauzero, A. P. Seitsonen, A. Smogunov, P. Umari, and R. M. Wentzcovitch, *Journal of Physics: Condensed Matter* **21**, 395502 (2009).

[48] P. Giannozzi, O. Andreussi, T. Brumme, O. Bunau, M. Buongiorno Nardelli, M. Calandra, R. Car, C. Cavazzoni, D. Ceresoli, M. Cococcioni, N. Colonna, I. Carnimeo, A. Dal Corso, S. de Gironcoli, P. Delugas, R. A. DiStasio, A. Ferretti, A. Floris, G. Fratesi, G. Fugallo, R. Gebauer, U. Gerstmann, F. Giustino, T. Gorni, J. Jia, M. Kawamura, H.-Y. Ko, A. Kokalj, E. Küçükbenli, M. Lazzeri, M. Marsili, N. Marzari, F. Mauri, N. L. Nguyen, H.-V. Nguyen, A. Otero-de-la Roza, L. Paulatto, S. Poncé, D. Rocca, R. Sabatini, B. Santra, M. Schlipf, A. P. Seitsonen, A. Smogunov, I. Timrov, T. Thonhauser, P. Umari, N. Vast, X. Wu, and S. Baroni, *Journal of Physics: Condensed Matter* **29**, 465901 (2017).

[49] F. Ma, S. Zhang, and H. Krakauer, *Phys. Rev. B* **95**, 165103 (2017).

[50] D. R. Hamann, <http://www.mat-simresearch.com/>.

[51] X. Gonze, J.-M. Beuken, R. Caracas, F. Detraux, M. Fuchs, G.-M. Rignanese, L. Sindic, M. Verstraete, G. Zerah, F. Jollet, M. Torrent, A. Roy, M. Mikami, P. Ghosez, J.-Y. Raty, and D. Allan, *Computational Materials Science* **25**, 478 (2002).

[52] S. Zhang, J. Carlson, and J. E. Gubernatis, *Phys. Rev. B* **55**, 7464 (1997).

[53] H. F. Trotter, *Proc. Amer. Math. Soc.* **10**, 545 (1959).

[54] M. Suzuki, *Communications in Mathematical Physics* **51**, 183 (1976).

[55] D. Thouless, *Nuclear Physics* **21**, 225 (1960).

[56] D. Thouless, *Nuclear Physics* **22**, 78 (1961).

[57] D. R. Hamann and S. B. Fahy, *Phys. Rev. B* **41**, 11352 (1990).

[58] J. Hubbard, *Phys. Rev. Lett.* **3**, 77 (1959).

[59] R. L. Strattonovich, *Dokl. Akad. Nauk SSSR* **115**, 1097 (1957).

[60] S. Zhang, J. Carlson, and J. E. Gubernatis, *Phys. Rev. B* **55**, 7464 (1997).

[61] W. Purwanto and S. Zhang, *Phys. Rev. E* **70**, 056702 (2004).

[62] S. Chen, M. Motta, F. Ma, and S. Zhang, *Phys. Rev. B* **103**, 075138 (2021).

[63] R. dos Santos, *Brazilian Journal of Physics* **33** (2003).

[64] J. Liu and L. Cheng, *The Journal of Chemical Physics* **148**, 144108 (2018).

[65] B. Zhang, J. E. Vandezande, R. D. Reynolds, and H. F. I. Schaefer, *Journal of Chemical Theory and Computation* **14**, 1235 (2018), pMID: 29461828.

[66] L. Visscher and K. G. Dyall, *The Journal of Chemical Physics* **104**, 9040 (1996).

[67] K. P. Huber and G. Herzberg, (Springer New York, NY, 1979).

[68] H. Kwee, S. Zhang, and H. Krakauer, *Phys. Rev. Lett.* **100**, 126404 (2008).

[69] F. Ma, S. Zhang, and H. Krakauer, *Phys. Rev. B* **84**, 155130 (2011).

[70] K. A. Peterson, D. Figgen, E. Goll, H. Stoll, and M. Dolg, *The Journal of Chemical Physics* **119**, 11113 (2003).

[71] M. Schlipf and F. Gygi, *Computer Physics Communications* **196**, 36 (2015).

[72] L. Brewer, (Lawrence Berkeley National Laboratory, 1977).

[73] H. J. Monkhorst and J. D. Pack, *Phys. Rev. B* **13**, 5188 (1976).

[74] A. Baldereschi, *Phys. Rev. B* **7**, 5212 (1973).

[75] R. W. G. Wyckoff, (Wiley, 1963).

[76] C. S. Menoni and I. L. Spain, *Phys. Rev. B* **35**, 7520 (1987).

[77] A. Mujica, A. Rubio, A. Muñoz, and R. J. Needs, *Rev. Mod. Phys.* **75**, 863 (2003).

[78] A. Baida and M. Ghezali, *Computational Condensed Matter* **17**, e00333 (2018).

[79] O. Arbouche, B. Belgoumène, B. Soudini, Y. Azzaz, H. Bendaoud, and K. Amara, *Computational Materials Science* **47**, 685 (2010).

[80] L. Schimka, J. Harl, and G. Kresse, *The Journal of Chemical Physics* **134**, 024116 (2011).

[81] S. B. Zhang and M. L. Cohen, *Phys. Rev. B* **35**, 7604 (1987).

[82] J. P. Perdew, K. Burke, and M. Ernzerhof, *Phys. Rev. Lett.* **77**, 3865 (1996).

[83] F. D. Murnaghan, *Proceedings of the National Academy of Sciences* **30**, 244 (1944).